


Strategies for accessing the multipulse regime of mode-locked fiber lasers

P. Tchofo Dinda,^{*} A. Malfondet, P. Grelu, and G. Millot[†]

Laboratoire Interdisciplinaire Carnot de Bourgogne, UMR No. 6303, CNRS, Université de Bourgogne, 9 Avenue A. Savary, BP 47870, 21078 Dijon Cedex, France

A. Kamagate 

Département de Mathématiques-Physique-Chimie, Université de Peleforo Gon Coulibaly, BP 1328, Korhogo, Côte d'Ivoire



(Received 5 December 2022; accepted 1 March 2023; published 21 March 2023)

Important ongoing research on mode-locked fiber lasers aims at developing new types of multisoliton regimes, such as soliton molecules, molecular complexes, or soliton crystals. The on-demand generation of such multipulse structures is a major challenge, whereas experiments generally involve a tedious trial-and-error adjustment of the laser parameters. Here we present an approach based on a gradual and calibrated adjustment of the system configuration, which employs efficient parameter routes to reach well-defined multipulse regimes. Our numerical simulations show that once the mode-locking threshold is reached, we can adjust the laser parameters gradually to force the evolution of the laser dynamics towards multipulse structures with fewer distortion in their intensity profiles, which are accessible at reduced pump power levels.

DOI: [10.1103/PhysRevA.107.033513](https://doi.org/10.1103/PhysRevA.107.033513)

I. INTRODUCTION

Mode-locked fiber lasers (MLFLs) are highly valued for their ability to generate pulses whose intensity profiles can be shaped by using tunable intracavity components such as saturable absorbers, phase masks, dispersion compensators, or optical filters. However, the deterministic shaping of complex multiple-pulse profiles remains a major challenge. These complex waveforms notably include soliton molecules [1–7], macromolecules [8–10], molecular complexes [11,12], and soliton crystals [13,14]. Soliton molecules, namely, compact aggregates of a few pulses bound by phase-sensitive interactions, are currently attracting a great deal of attention for their potential applications in optical information encoding. Such applications require the generation of on-demand soliton molecules, which involves complex control of intracavity parameters [15,16]. However, to generate any of these complex multipulse structures, the first task is to efficiently access the multipulse regime of the laser. The pumping power (PP) is the most accessible and determining cavity parameter in that process. The mode-locking threshold is defined as the minimum PP needed to access any short-pulse regime. When this threshold is reached, we assume that the laser generates a single pulse inside the cavity. This condition is not always met, in particular for fiber laser setups designed for a low pulse energy and high-harmonic mode-locking operation [17,18]. Nevertheless, we can assume that this is generally the case for a fiber laser designed to generate just a few pulses. After the single-pulse regime is reached, by increasing the PP further, a

multipulsing instability develops so that the laser switches to the multipulse regime [19–24]. In the following, we will refer to this common procedure of accessing the multipulse regime as the conventional approach.

In some laser configurations, the PP needed to generate multipulse structures can be much higher than the mode-locking threshold so that the pulses can be subjected to significant distortions in their intensity profile [25]. The framework of dissipative solitons explains how the field profile of any stable pulse structure is strongly affected by a combination of dispersive and dissipative, linear and nonlinear, propagation effects [9]. Spectral filtering is one of the most important effects, which affects the overall laser dynamics and the stationary pulse profile. Whereas the finite bandwidth of the gain profile of the doped fiber has already an important effect on the pulsed laser dynamics [26,27], its impact can be strongly enhanced if a bandpass filter (BPF) with a bandwidth lower or of the same order as that of the gain bandwidth is inserted into the cavity [28–31]. Therefore, many previous studies have used BPFs to modify the laser dynamics. For instance, it has been shown that BPFs can be used to design MLFLs with large tunability capabilities, such as the ability to adjust the pulse wavelength [32], adjust separately the wavelength and the temporal width of pulses [33–35], stretch and compress the pulses in the temporal domain [36,37], or compress the pulses in the spectral domain to generate their fragmentation [23,24,38,39]. Another class of applications of filtering is to sculpt the intensity profile of stable states such as parabolic-, flat-top-, triangular-, and sawtooth-profiled pulses [40–42], dispersion-managed soliton profiles [43], similaritons [39], and rogue waves [44]. At this point, we need to raise the issue of hysteresis and multistability, where in regions of the parameter space, the laser can generate several distinct stable states corresponding

^{*}tchofo@u-bourgogne.fr

[†]Also at Institut Universitaire de France, 1 Rue Descartes 75005 Paris, France.

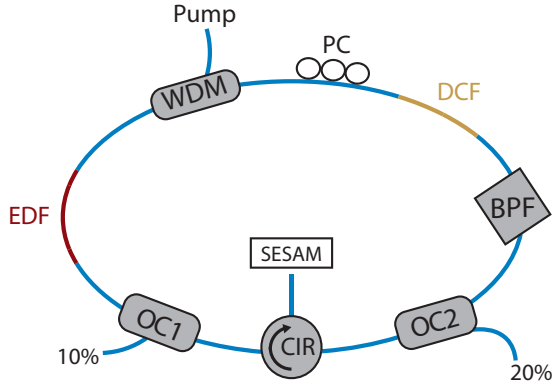


FIG. 1. Schematic of the fiber laser cavity.

to the same cavity parameters [20]. The access to one of the stable states at a given time depends on the dynamical trajectory followed by the laser when the cavity parameters are varied to reach their target values. In most experiments, such trajectories are not known in advance, which is why a trial and error procedure generally precedes the generation of complex multipulse structures.

In the present study we consider a MLFL with adjustable pulse generation capacities provided by two tunable laser components: an erbium-doped fiber amplifier (EDFA) and a BPF with tunable bandwidth. We show that by following a specific procedure to adjust the PP of the EDFA and the bandwidth of the BPF, the laser dynamics follows a trajectory leading to stable multipulse states with predefined properties. In comparison with situations where the conventional approach causes huge distortions in the pulse's intensity profile, we demonstrate here that our procedure allows us to reach a multipulse regime and generate pulses without profile distortions, at reduced pump power. Our approach is simple to implement as it combines tunable components commercially available.

II. NUMERICAL MODELING

Our laser model is a unidirectional ring cavity that combines the following four major components placed in the order indicated in Fig. 1: a BPF with tunable bandwidth, a section of dispersion-compensating fiber (DCF) to adjust the average cavity dispersion, a section of erbium-doped fiber (EDF) pumped by a laser diode through a wavelength division multiplexing (WDM) coupler, and a semiconductor saturable absorber mirror (SESAM) used to insert nonlinear losses and favor laser mode locking. Two output couplers (OCs), labeled OC1 and OC2, respectively, are inserted into the cavity. The coupler OC1 is placed after the output of the EDFA, where the pulse energy is maximum for the user. The coupler OC2, placed at the input of the BPF, is used to characterize the pulse before its passage through the BPF. A circulator (CIR) is placed between the couplers OC1 and OC2 to receive the light reflected by the SESAM and inject it back into the cavity. The circulator also imposes a unidirectional propagation of light through the cavity. Since all components are spliced to single-mode fibers (SMFs), the cavity is thus equipped with an active fiber and a number of sections of SMF. In our scalar model,

the pulse propagation in these fiber sections can be described by the generalized nonlinear Schrödinger equation (GNLSE) [23,45,46]

$$\begin{aligned} \psi_z + \frac{i\beta_2}{2}\psi_{tt} - \frac{\beta_3}{6}\psi_{ttt} + \frac{\alpha - g(z, P_{av}, \nu_s)}{2}\psi \\ = i(1 - \rho)\gamma|\psi|^2\psi + R[\psi], \end{aligned} \quad (1)$$

where β_2 , β_3 , γ , g , and α designate the second-order dispersion (SOD), third-order dispersion (TOD), Kerr nonlinearity, gain, and linear attenuation parameters, respectively. The term $R[\psi]$, which describes the Raman effect, is written as [46] $R[\psi] = i\gamma\rho\psi\int_0^\infty\chi_R(s)|\psi|^2(t-s)ds$, where χ_R represents the Raman susceptibility and ρ is the fractional contribution of the Raman scattering to the total nonlinearity, with $\rho = 0.18$ [46]. In Eq. (1), $g = 0$ in the case of the passive fiber sections (SMF), whereas for the active fiber (EDF) $g(z, P_{av}, \nu_s)$ is calculated at any signal frequency ν_s , from the rate equations for the pump and signal power at a given longitudinal position z along the active fiber [23]. Here P_{av} is the average power at the input facet of the EDF. The value of P_{av} is related to the total field energy E as $P_{av} \equiv E(z)/\tau_{rt} = \frac{1}{\tau_{rt}}\int|\psi(t, z)|^2dt$, where τ_{rt} designates the cavity round-trip time. The GNLSE (1) is numerically solved by means of the split-step Fourier method [45].

The action of the SESAM on an incident light field is modeled as instantaneous. This would correspond in practice to a SESAM with a subpicosecond response time applied on picosecond laser pulses. It is modeled by the monotonic transfer function for the optical power

$$P_o = TP_i, \quad (2a)$$

$$T \equiv T_0 + \frac{\Delta TP_i}{P_i + P_{sat}}, \quad (2b)$$

where T describes the transmission of the instantaneous saturable absorber (SA), T_0 is its transmittivity at low signal, ΔT is the absorption contrast, and P_i (P_o) designates the instantaneous input (output) optical power.

The BPF spectral profile is modeled by the super-Gaussian function $F_{BPF}(\omega) = \exp[-2^{2m}\log(2)\frac{\omega^{2m}}{\Delta\Omega_{BPF}^{2m}}]$, where $\Delta\Omega_{BPF}$ is the filter's bandwidth and m is an integer that determines the filter's profile. The value $m = 1$ corresponds to a Gaussian profile, whereas for $m > 1$ the BPF's profile has an increasingly flat top and steeper flanks as m increases. Throughout the present work, we model the flat-top filter with $m = 4$. The other lumped elements of the laser cavity (coupler and splices) only induce broadband linear losses.

Our numerical simulations are performed using the following parameters: (i) an EDF with SOD of $-15 \text{ ps nm}^{-1} \text{ km}^{-1}$, TOD of approximately $0 \text{ ps nm}^{-2} \text{ km}^{-1}$, effective mode area equal to $28.3 \text{ } \mu\text{m}^2$, length equal to 1.2 m , and loss equal to 0.2 dB/km ; (ii) a SMF with SOD of $18 \text{ ps nm}^{-1} \text{ km}^{-1}$, TOD of $0.07 \text{ ps nm}^{-2} \text{ km}^{-1}$, effective mode area equal to $78.5 \text{ } \mu\text{m}^2$, total length equal to 15.81 m , and loss equal to 0.2 dB/km ; (iii) a DCF with SOD of $-91.7 \text{ ps nm}^{-1} \text{ km}^{-1}$, TOD of $-0.12 \text{ ps nm}^{-2} \text{ km}^{-1}$, effective mode area equal to $20 \text{ } \mu\text{m}^2$, length equal to 2.9 m , and loss equal to 0.6 dB/km ; (iv) a saturable absorber with $T_0 = 0.7$ (70%), $\Delta T = 0.3$ (30%), and $P_{sat} = 10 \text{ W}$; and (v) output coupler transmissions OC1 (90%) and OC2 (80%).

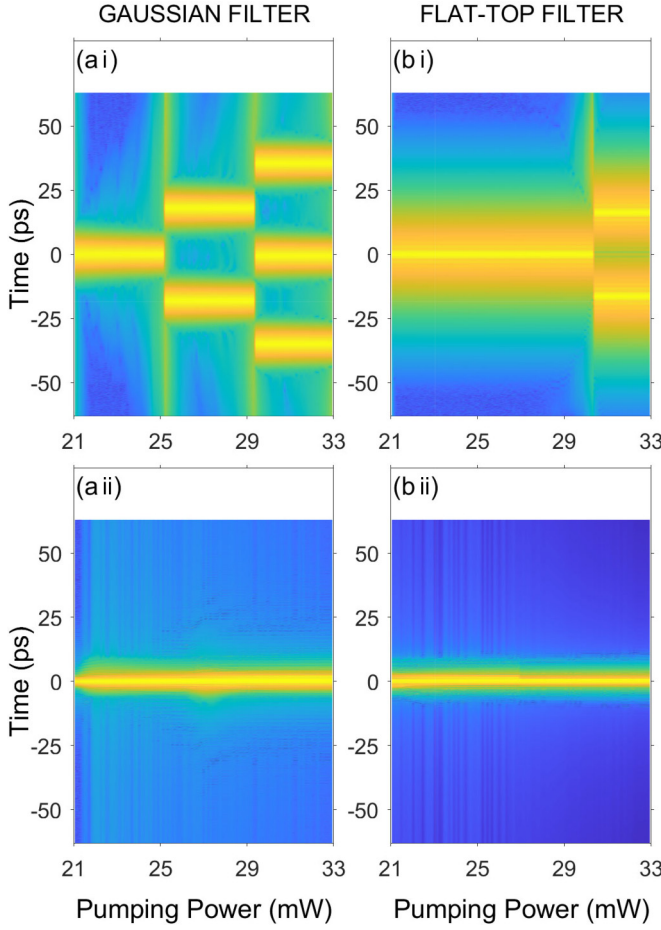


FIG. 2. Evolution in color scale of the temporal intracavity intensity as a function of the pumping power for (a i) and (b i) $\Delta\lambda = 4$ nm and (a ii) and (b ii) $\Delta\lambda = 12$ nm.

III. CONVENTIONAL PROCEDURE OF ACCESS TO THE MULTIPULSE REGIME

The conventional approach to access the multipulse regime of a MLFL is to first adjust the laser PP slightly above the mode-locking threshold to generate a single pulse in the cavity. Then the PP is increased gradually until the single pulse present in the cavity becomes unstable and fragments into two (or more) pulses. Figure 2 illustrates, in color scale, the evolution of the temporal intensity of the intracavity electric field recorded at the input of the BPF, when the PP is increased from 21 mW to 33 mW. Figure 2(a i) shows that in a cavity equipped with a BPF of 4 nm bandwidth, the switch to the multipulse regime occurs at a PP of 25.6 mW, which leads to the fragmentation of the initial pulse into two pulses. By continuing to increase the PP, a new fragmentation process occurs at 29.3 mW, followed by a restructuring of the intracavity field into three pulses. The behavior observed for the cavity equipped with a BPF of 4 nm bandwidth [Fig. 2(a i)] differs drastically from that shown in Fig. 2(a ii) corresponding to a bandwidth of 12 nm. Indeed, in the same PP range, i.e., between 21 and 33 mW, the multipulse regime is inaccessible with a 12-nm-bandwidth filter. Comparison between the results of Figs. 2(a i) and 2(b i) shows that for $\Delta\lambda = 4$ nm,

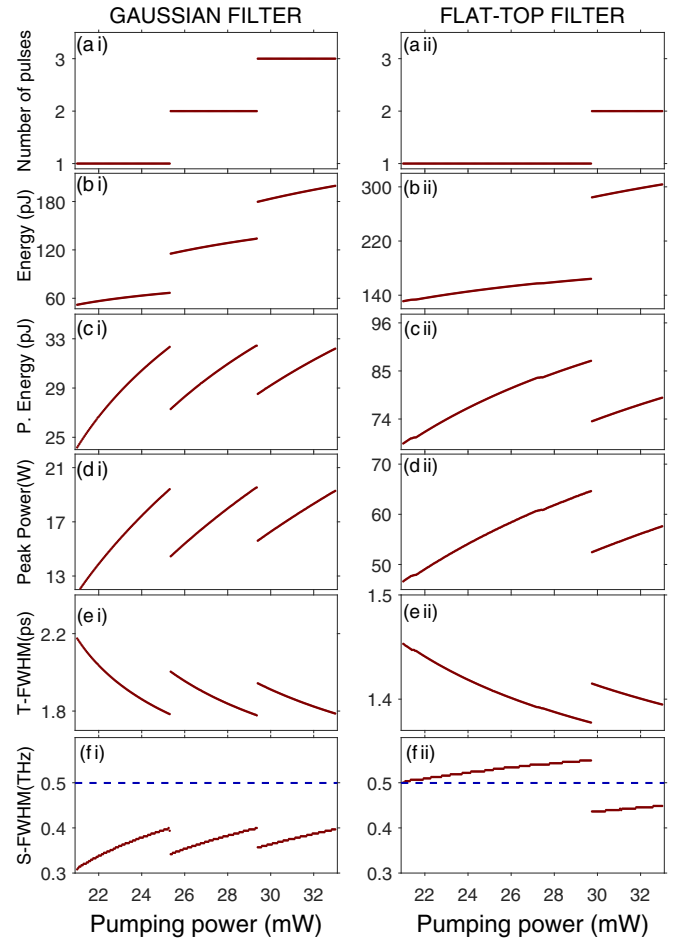


FIG. 3. Evolution of the pulse parameters as a function of the pumping power for $\Delta\lambda = 4$ nm. The pulse parameters are calculated from the pulse profile at the BPF input: (a i) and (a ii) number of pulses generated, (b i) and (b ii) total energy of the intracavity field, (c i) and (c ii) pulse energy, (d i) and (d ii) pulse peak power, (e i) and (e ii) temporal FWHM of the peak intensity, and (f i) and (f ii) spectral FWHM.

the flat-top filter increases the PP transition to the multipulse regime and reduces the number of fragmentation points. For large filter bandwidths, there is no significant difference related to the type of filter spectral profile considered [see Figs. 2(a ii) and 2(b ii)].

Thus, the most striking feature of the conventional procedure for accessing the multipulse regime is the pulse fragmentation shown in Figs. 2(a i) and 2(b i). However, Fig. 2 gives no insight into the physical mechanism underlying the fragmentation process. To get an idea of this physical mechanism, we show in Fig. 3 the evolution of the main physical parameters of the pulse in the case considered in Figs. 2(a i) and 2(b i), where $\Delta\lambda = 4$ nm. Here and in the following, the pulse parameters are calculated using collective coordinate techniques [22,46]. Figures 3(b i) and 3(b ii) show that the total intracavity energy (including all pulses) increases monotonically with PP and makes a steep jump at each fragmentation point. Figures 3(c i) and 3(c ii) show that the pulse energy increases monotonically with PP and

falls sharply at each fragmentation point. The pulse's peak power evolves in the same way as the energy, as illustrated by Figs. 3(d i) and 3(d ii). Unlike the evolution of peak power, the temporal full width at half maximum (FWHM) of the peak intensity decreases monotonically as the PP increases and makes a sharp jump at each fragmentation point. This temporal narrowing of the pulse in the phase preceding the fragmentation point is in line with the widening the pulse spectrum, as shown by Figs. 3(f i) and 3(f ii). This turns out to be the essential pulse splitting mechanism: As we gradually increase the PP, the pulse spectrum widens to a critical point close to the filter bandwidth, where the action of the filter destabilizes and fragments the pulse. It should be noted that fragmentation mechanisms usually involve a well-defined limiting physical effect acting as a trigger for fragmentation. In Ref. [19] the fragmentation mechanism is basically based on the saturation of the nonlinear gain parameter or, equivalently, on an overdrive of the saturable absorber. Therefore, as an increase in pump power tends to produce higher-intensity pulses, such overdrive imprints a modulation at the top of these high-intensity pulses, leading to a breakup of the pulse. In contrast, in our laser cavity, the limiting physical effect leading to pulse fragmentation is the finite spectral window of the BPF that we manipulate at will. At higher pump power, excess self-phase modulation is converted into an increase in spectral width of the pulse, which is negatively discriminated by the BPF. Therefore, the localized and strong action of the BPF destabilizes the pulse and leads to its fragmentation. While these mechanisms operate in different parameter domains, they are not contradictory and are even likely to overlap, as each pulse parameter is related to the others by complex relationships created by linear and nonlinear effects modeled by the terms present in the GNLSE (1). This is also the reason why each fragmentation phenomenon causes a steep variation of the value of all pulse parameters (temporal width, spectral width, peak power, and chirp), as can be seen in Fig. 3. The fragmentation phenomenon is most clearly visible in Figs. 3(f i) and 3(f ii), where a sharp reduction in the pulse spectral width is observed. However, the specificity of the optical pulse is that it is subject to a condition of stability in the laser cavity, requiring a specific intensity profile to ensure the balance between the different physical phenomena present in the cavity (gain, loss, dispersion, nonlinearity, etc.). Therefore, at the point of fragmentation, the reduction of the spectral width of the pulse is necessary but not sufficient. A restructuring of the entire pulse profile is required to satisfy the stability condition in the cavity, hence the abrupt change in all the physical parameters of the pulse, which is comparable to a relaxation process leading to pulse reconfinement in the filter bandwidth.

On the other hand, Figs. 3(f i) and 3(f ii) highlight a major difference between the two types of filters in their way of shaping the pulse intensity profile. Indeed, we see in Fig. 3(f i) that the Gaussian filter acts in such a way as to confine the pulse spectrum strictly within its FWHM bandwidth (indicated by the horizontal dashed line). Quite unexpectedly, despite its steep flanks, the flat-top filter leads to pulses whose spectrum clearly exceeds the FWHM filter bandwidth, as shown in Fig. 3(f ii). This bandwidth overflow reaches its maximum just before the fragmentation point, i.e.,

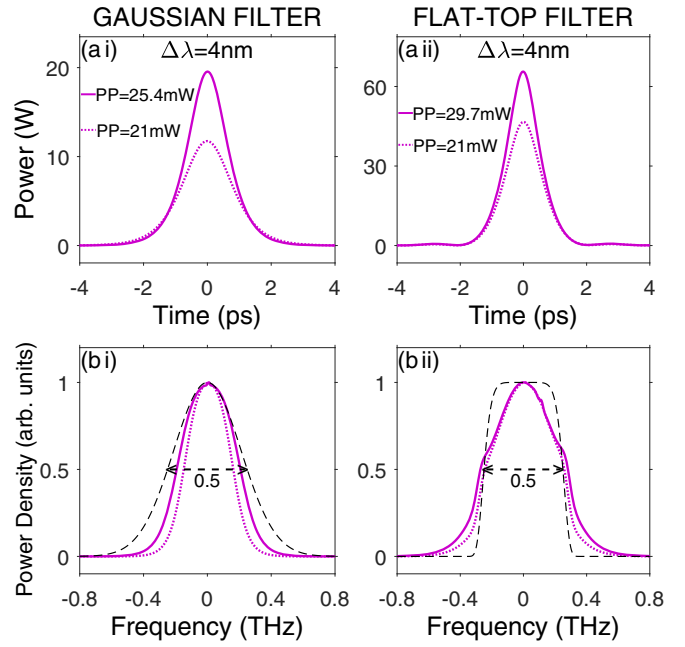


FIG. 4. Pulse intensity profile just before the first fragmentation point for the cavity considered in Fig. 2: (a i) and (a ii) temporal profile and (b i) and (b ii) spectral profile. The dotted curve shows for comparison the pulse profile for a pumping power well before this fragmentation point.

at 29.7 mW. This phenomenon, which was also reported in Ref. [27], is even clearer in Fig. 4, in which the solid curves represent the intensity profiles recorded at the filter input just before the first fragmentation point, i.e., at a power of 25.3 mW (29.7 mW) for the Gaussian (flat-top) filter. In Figs. 4(b i) and 4(b ii) the dashed curves represent the spectral profile of the filter, with a bandwidth of 4 nm (equivalent to 0.5 THz). The dotted curves in Fig. 4 illustrate the fact that the pulse spectrum does not exceed the limits of the filter bandwidth when the PP is sufficiently far from the first fragmentation point. As the PP rises and approaches the fragmentation point, the pulse spectrum widens but without crossing the bandwidth limits of a Gaussian filter, while there is an overflow of the bandwidth in the cavity equipped with the flat-top filter. In addition, careful examination of Figs. 4(a i) and 4(b i) reveals that the Gaussian filter favors the generation of pulses whose intensity profile has a bell curve shape, while the flat-top filter inflicts slight profile distortions, which are more visible in Fig. 4(b ii) than in Fig. 4(a ii).

In Fig. 3 we have highlighted the evolution of the pulse parameters as a function of PP, but with parameters evaluated at a specific point of the cavity, i.e., at the BPF input. As we consider a dispersion-managed cavity, i.e., a cavity where we have inserted a DCF in order to obtain an average cavity dispersion value close to zero, the pulse parameters are likely to vary substantially over a cavity round-trip. The knowledge of this pulse's internal dynamics is useful to appreciate the respective roles of the different components of the cavity in the structuring of the stable states of the laser. The solid line curves in Fig. 5 illustrate the intracavity dynamics of the pulse parameters for a PP just before the fragmentation

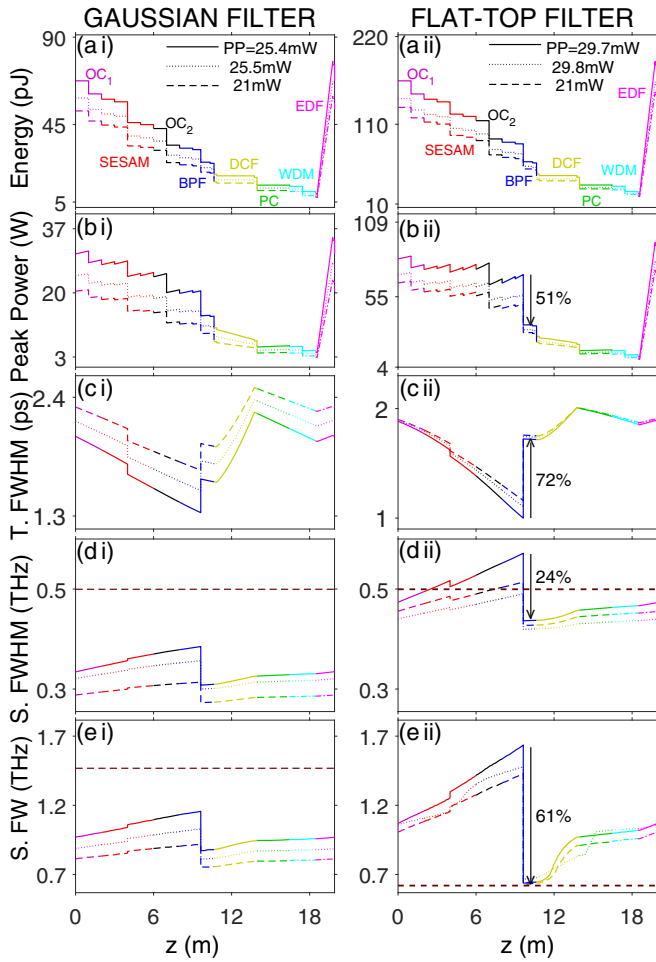


FIG. 5. Evolution of the pulse parameters over a round-trip in the cavity for $\Delta\lambda = 4$ nm: (a i) and (a ii) pulse energy, (b i) and (b ii) pulse peak power, (c i) and (c ii) temporal FWHM, (d i) and (d ii) spectral FWHM, and (e i) and (e ii) spectral FW.

point, while the dotted curves illustrate the dynamics just after the fragmentation point. The dashed curves show the internal dynamics for a PP located well before the fragmentation point. Note that the curves of evolution of the energy and the peak power contain a number of small jumps corresponding to the linear losses between the different components of the laser. More importantly, Fig. 5 highlights the following major points.

(i) The PP located just before the fragmentation point (i.e., 25.4 and 29.7 mW for the Gaussian and flat-top filters, respectively) is the operating condition of the cavity for which the internal dynamics is strongest, as remarkably illustrated by Figs. 5(b ii), 5(c ii), 5(d ii), and 5(e ii), where we see that at each pass, the flat-top filter dramatically changes the pulse intensity profile, causing a drop of 51% in its peak power, a jump of 72% in its temporal FWHM, a drop of 24% in its spectral FWHM, and a drop of 61% in its spectral full width (FW). Here and in the following, the FW is defined as the width at 1% of the maximum. This operating condition is also the one that exacerbates the bandwidth overflow phenomenon, because here the overflow relates to the pulse's spectral FWHM. Indeed, Fig. 5(d ii) shows that over a distance

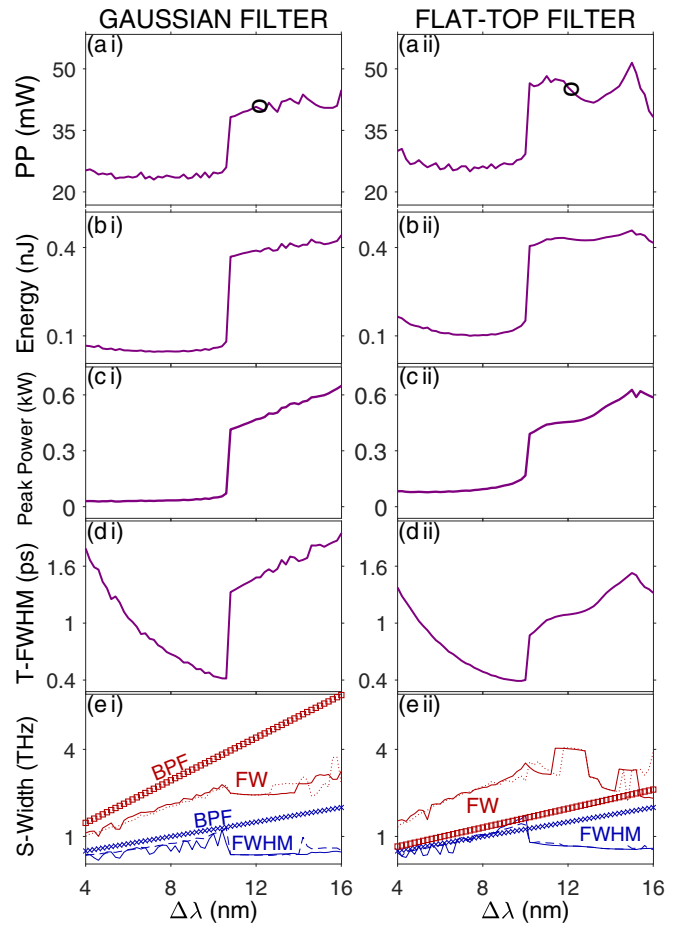


FIG. 6. Access to the multipulse regime through the conventional approach: (a i) and (a ii) PP of access to the multipulse regime as a function of filter bandwidth, (b i) and (b ii) total energy of the intracavity field, (c i) and (c ii) peak power, (d i) and (d ii) temporal width, and (e i) and (e ii) spectral width.

from $z = 2.25$ m to the entrance of the flat-top filter located at $z = 9.63$ m (which corresponds to almost one-third of the length of the cavity), the spectral width of the pulse is clearly beyond the filter bandwidth.

(ii) The dotted curves in Fig. 5 show that a relaxation of the internal dynamics occurs just after the fragmentation point, with a major effect visible in Fig. 5(d ii), which is to bring the spectral dynamics of the pulse back within the bandwidth of the system. On the other hand, relaxation does not suppress the spectral overflow as far as the spectral FW is concerned, as can be seen from Fig. 5(e ii), which shows that there is overflow of bandwidth over almost the entire length of the cavity, except for a distance of about 2 m after crossing the flat-top filter.

As we have seen in Fig. 2, the PP of access to the multipulse regime via the conventional approach, defined as the first point of fragmentation, differs quantitatively depending on whether $\Delta\lambda = 4$ or 12 nm. To have a more in-depth idea of the influence of filter bandwidth, we gradually raised the PP from the mode-locking threshold to the first fragmentation point, for different values of $\Delta\lambda$ between 4 and 12 nm. The result is visible in Fig. 6, where Fig. 6(a i) shows the value

of PP as a function of filter bandwidth, while the other panels represent the pulse parameters just before the fragmentation point. Figures 6(a i) and 6(a ii) show that the evolution curve of the PP roughly resembles a two-level staircase. The resulting intracavity energy also has an evolution curve that resembles a staircase, as shown in Figs. 6(b i) and 6(b ii). In Figs. 6(a i) and 6(a ii) we observe that the PP varies only very slightly over a wide range of values of $\Delta\lambda$ ranging from 4 nm to some critical value, say, $\Delta\lambda_c$, which is about 11 nm. As soon as $\Delta\lambda$ exceeds $\Delta\lambda_c$, the PP abruptly jumps to a level that is almost double the PP level in the region $\Delta\lambda < \Delta\lambda_c$. However, we observe that in the region where $\Delta\lambda > \Delta\lambda_c$, the PP fluctuates much more than in the region $\Delta\lambda < \Delta\lambda_c$. These large fluctuations in PP reflect less stability of the pulse, which can result from the combination of several factors. The first is the dramatic increase in nonlinearity induced by the high level of the pulse's peak power, which is an order of magnitude higher than that we observe for $\Delta\lambda < \Delta\lambda_c$, as shown in Figs. 6(c i) and 6(c ii). The second factor is probably related to the filtering effect induced by the gain curve of the active fiber, which is expected to come into play when the filter bandwidth is sufficiently large, i.e., in the region $\Delta\lambda > \Delta\lambda_c$. Unlike our BPF whose bandwidth is manually adjustable in a way completely independent of the operating conditions of the laser, the filtering induced by the gain curve of the active fiber is very sensitive to the average power of the optical field at the input of the active fiber, which is itself highly dependent on the pumping power of the active fiber. More importantly, one can raise the question of the physical origin of the critical behavior occurring at $\Delta\lambda = \Delta\lambda_c$. The answer to this question can be obtained by carefully examining the evolution curves of the pulse spectral widths in Figs. 6(e i) and 6(e ii). In these figures the lines represented by small crosses and diamonds represent the filter bandwidth at the FWHM and at the FW, respectively. Indeed, we observe for $\Delta\lambda < \Delta\lambda_c$ that the spectral width of the generated pulses follows almost the same ascending curve as that of the filter, thus indicating that the filter plays a crucial role in shaping the pulse profile. Beyond $\Delta\lambda_c$, the pulse spectral width stops growing, thus indicating that the BPF no longer plays a significant role in intracavity dynamics, and consequently the filtering effect induced by the gain curve of the active fiber comes into play. However, in our cavity, there is no way to control this filtering effect. The main features of the conventional procedure for accessing the multipulse regime of a MLFL are remarkably illustrated in Fig. 7, which shows the intensity profiles of the stable states obtained for $\Delta\lambda = 8$ and 12 nm, respectively, which correspond to two bandwidth values located below and above, respectively, the critical value $\Delta\lambda_c \sim 11$ nm revealed in Fig. 6. It should be recalled that for each of the two values of $\Delta\lambda$ considered, the procedure consists in gradually increasing the PP to a value slightly above the fragmentation point. Figures 7(a i) and 7(b i) and Figs. 7(a ii) and 7(b ii) clearly illustrate that for $\Delta\lambda = 8$ nm $< \Delta\lambda_c$, the multipulse state consists of pulses whose intensity profile has a nice bell-shaped curve, without significant distortions. On the contrary, for $\Delta\lambda > \Delta\lambda_c$, the pulse profiles are affected by very severe distortions, as is clearly shown by the insets in Figs. 7(a iii) and 7(a iv). We attribute those profile distortions to the nonlinear effects induced by the much larger pulse's peak power in the region

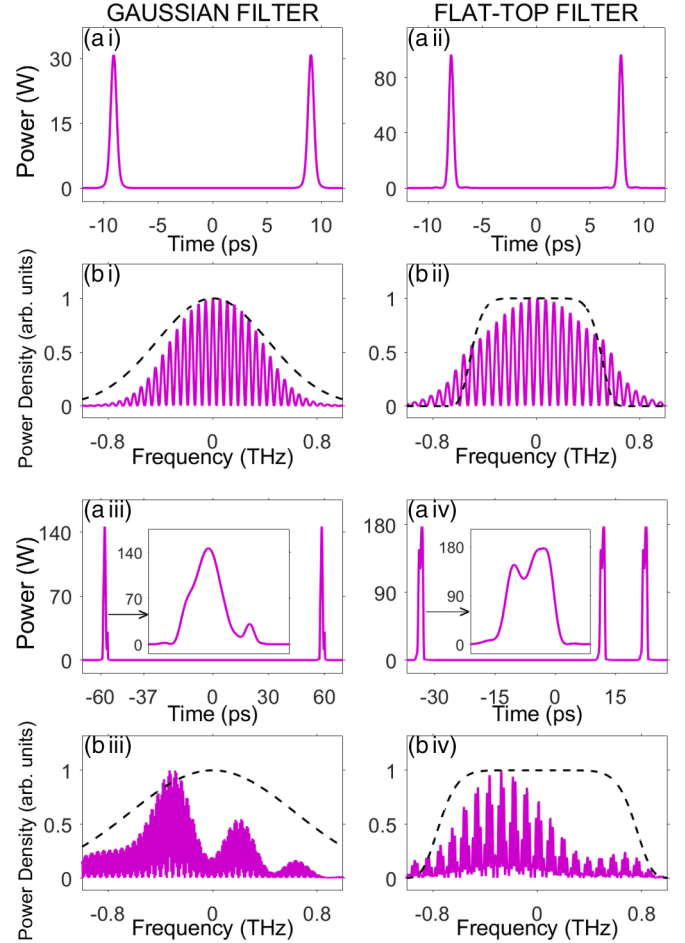


FIG. 7. Multipulse intensity profile obtained by the conventional approach, for a PP slightly above the first fragmentation point: (a i) and (b i) multipulse profile for $\Delta\lambda = 8$ nm and PP equal to 25 mW for the cavity with a Gaussian filter, (a ii) and (b ii) multipulse profile for $\Delta\lambda = 8$ nm and PP equal to 28 mW for the cavity with a flat-top filter, (a iii) and (b iii) multipulse profile for $\Delta\lambda = 12$ nm and PP equal to 49 mW for the cavity with a Gaussian filter, and (a iv)-(b iv) multipulse profile for $\Delta\lambda = 12$ nm and PP equal to 50 mW for the cavity with a flat-top filter.

$\Delta\lambda > \Delta\lambda_c$ (which is nearly twice as much as that of the pulses generated when $\Delta\lambda < \Delta\lambda_c$). Those profile distortions result from the high level of PP required to reach the multipulse regime, which is almost double the PP required when $\Delta\lambda < \Delta\lambda_c$. In the following section we present a procedure for accessing the multipulse regime, which avoids the two disadvantages arising from the conventional approach.

IV. ACCESSING THE MULTIPULSE REGIME VIA A TWO-DIMENSIONAL PARAMETER APPROACH

In the preceding section we analyzed the conventional procedure for accessing the multipulse regime of MLFLs through the use of the PP as the only control parameter beyond the mode-locking threshold. On the other hand, we have highlighted in Fig. 6 the major influence of the BPF's bandwidth on the PP that is needed to access the multipulse regime. The peculiarity of our two-dimensional (2D) procedure for

accessing the multipulse regime is to use the BPF's bandwidth $\Delta\lambda$ as a system configuration parameter, in the same way as the PP. In this procedure, we move the PP and adjust the filter's bandwidth so as to minimize the PP needed to reach the multipulse regime. As we can see in Fig. 6(a i), in the conventional approach, the PP for accessing the multipulse regime is minimal for a filter bandwidth below $\Delta\lambda_c$, while for $\Delta\lambda > \Delta\lambda_c$ the PP is about twice higher. Therefore, the 2D approach should be particularly useful for easy access to the multipulse regime in cavities where $\Delta\lambda > \Delta\lambda_c$. To illustrate this procedure, consider again the laser cavity configured with a bandwidth of 12 nm while keeping in mind that for $\Delta\lambda = 12$ nm the PP required to access the multipulse regime is greater than 40 mW when the conventional approach is used, as indicated by the small circles in Figs. 6(a i) and 6(a ii). Our 2D approach takes place in two steps.

(i) First, we set the filter bandwidth to a value $\Delta\lambda_{\text{opt}} \neq \Delta\lambda$ for which the multipulse regime is easily accessible by the conventional approach, i.e., accessible with the lowest possible PP. Then, from the mode-locking threshold, we gradually increase the PP up to the value P_{PF} where fragmentation occurs. In the second step of the two-dimensional procedure, the PP is maintained at the value P_{PF} .

(ii) The second step begins with a laser already in the multipulse regime but with a bandwidth $\Delta\lambda_{\text{opt}} \neq \Delta\lambda$. Here the procedure consists of gradually increasing the filter's bandwidth from $\Delta\lambda_{\text{opt}}$ to $\Delta\lambda$. We emphasize that such bandwidth adjustment must be done gradually in order to prevent the laser from exiting the multipulse regime.

Figures 8(a i) and 8(a ii) show the results obtained using the 2D approach described above, starting the first step of the procedure with $\Delta\lambda_{\text{opt}} = 8$ nm and ending just after the fragmentation point, at a PP of 24.50 mW (27.35 mW) for the cavity equipped with a Gaussian (flat-top) filter. Note that in Fig. 8 and all subsequent figures, the intracavity field is recorded at the BPF input. Thus, Figs. 8(a i) and 8(a ii) show that the first step of our 2D approach results in the generation of two pulses in the cavity, in a similar way to the conventional approach. In the second step of the procedure, we gradually increase the bandwidth from 8 nm to 12 nm. However, in Fig. 8(a i), during this operation, the two pulses remain stable up to a certain value of $\Delta\lambda$ close to 12 nm, where a *defragmentation* phenomenon occurs and restructures the intracavity field so as to produce a single pulse in the cavity. Note that defragmentation is not clearly visible in Fig. 8(a i) because it occurs at the very end of the wavelength range considered, i.e., 11.97 nm. Thus, in Fig. 8(a i) our goal of accessing the multipulse regime in a cavity with a bandwidth of 12 nm was not achieved by finally setting the PP to the level just after the fragmentation point in the first step of the procedure. In this context, the question arises as to whether we could access the multipulse regime by completing the first phase at a PP slightly greater than the fragmentation point. The answer to this question is given in the Fig. 8(b i), where it is observed that, by ending the first step with a PP slightly above the fragmentation point, i.e., 25 mW, we finally access the multipulse regime with a filter of 12 nm of bandwidth, but here three pulses are generated within the cavity.

In contrast, Fig. 8(c i) shows that by ending the first step with a PP slightly below the fragmentation point, the laser

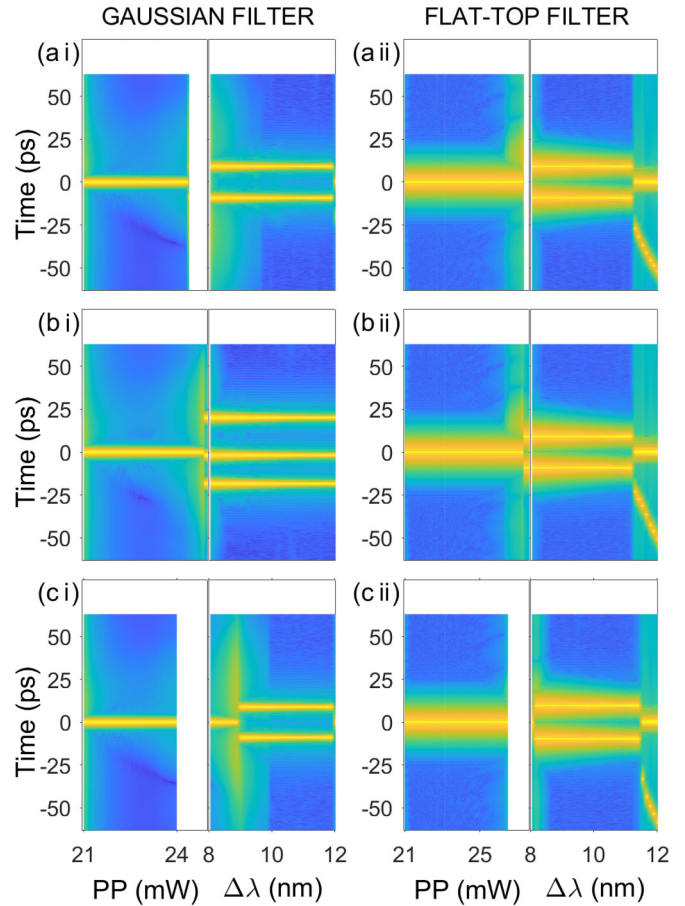


FIG. 8. Evolution of the temporal optical intensity along with the PP increase at $\Delta\lambda = 8$ nm (first step) and with the filter bandwidth increase at fixed PP (second step): (a) final PP set just after the fragmentation point at (a i) 24.5 mW and (a ii) 27.35 mW, (b) final PP set slightly above the fragmentation point at (b i) 25 mW and (b ii) 27.6 mW, and (c) final PP set slightly below the fragmentation point at (c i) 24 mW and (c ii) 26.5 mW.

enters the second phase of the 2D approach when it is still in single-pulse regime, but does not remain in this regime throughout the rest of this phase. Against all odds, despite the PP being below the fragmentation point, a fragmentation process occurs at a value of $\Delta\lambda \sim 9$ nm. The laser then enters a multipulse regime and remains there until $\Delta\lambda = 11.9$ nm, and there a defragmentation occurs [but without being clearly visible in Fig. 8(c i), much like in the case of Fig. 8(a i)] and brings the laser back into single-pulse mode. Furthermore, we see in Figs. 8(a ii), 8(b ii), and 8(c ii) that a cavity equipped with a flat-top filter shows a qualitative difference compared to a cavity equipped with a Gaussian filter. Indeed, in the three cases considered, i.e., a PP located just after the fragmentation point [Fig. 8(a ii)], slightly above the fragmentation point [Fig. 8(b ii)], and slightly below the fragmentation point [Fig. 8(c ii)], the laser enters a second multipulse regime that is nonstationary and comprises two pulses of unequal intensity. Such a phenomenon is not observed with the Gaussian filter, which generates stationary pulses of the same intensity [Fig. 8(b i)]. Figure 9 shows the intensity profile of the structure generated via the 2D procedure for accessing the

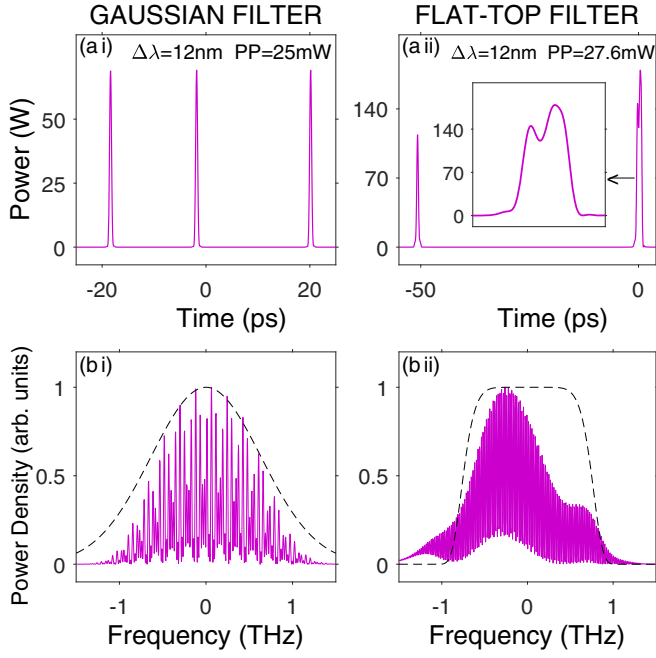


FIG. 9. Multipulse intensity profile generated at the end of the 2D procedure shown in Figs. 8(c i) and 8(c ii): (a i) and (a ii) temporal profile and (b i) and (b ii) spectral profile.

multipulse regime described in Fig. 8, highlighting a difference in the number of pulses generated, i.e., three pulses in the case of the Gaussian filter and two pulses for the flat-top filter.

We discovered in Fig. 8 that an undesirable phenomenon can occur during the configuration of the cavity by the 2D approach, namely, the defragmentation of the multipulse structure. Defragmentation appears as a critical phenomenon of restructuring of an intracavity field initially having a profile very far from that is really adapted to the configuration parameters of the cavity. In general, a restructuring phenomenon resulting in a change in the number of pulses within a laser cavity (fragmentation or defragmentation) is a very brief process during which the intracavity field executes fluctuations of large amplitude, temporarily requiring a large amount of energy. A gradual increase in PP naturally favors this type of process by an energy supply activated from outside the cavity. Now, in the second step of the 2D approach, we gradually increase the bandwidth of the BPF, which has the consequence of reconfiguring the cavity towards the single-pulse regime. However, by keeping PP at a fixed level, we also deprive the cavity of an energy source capable of promoting a huge restructuring of the intracavity field. This is the reason why the system remains in multipulse mode over a wide range of values of $\Delta\lambda$ before switching back to the single-pulse regime, which we here call defragmentation. Defragmentation also temporarily requires a supply of energy to the intracavity field, which is possible by self-organization of the internal dynamics of the intracavity field so as to minimize the absorption induced by the saturable absorber (SESAM) while increasing the intracavity gain (which depends not only on the PP but also on the average power of the field at the input of the EDF). In this internal dynamic, the intracavity field can

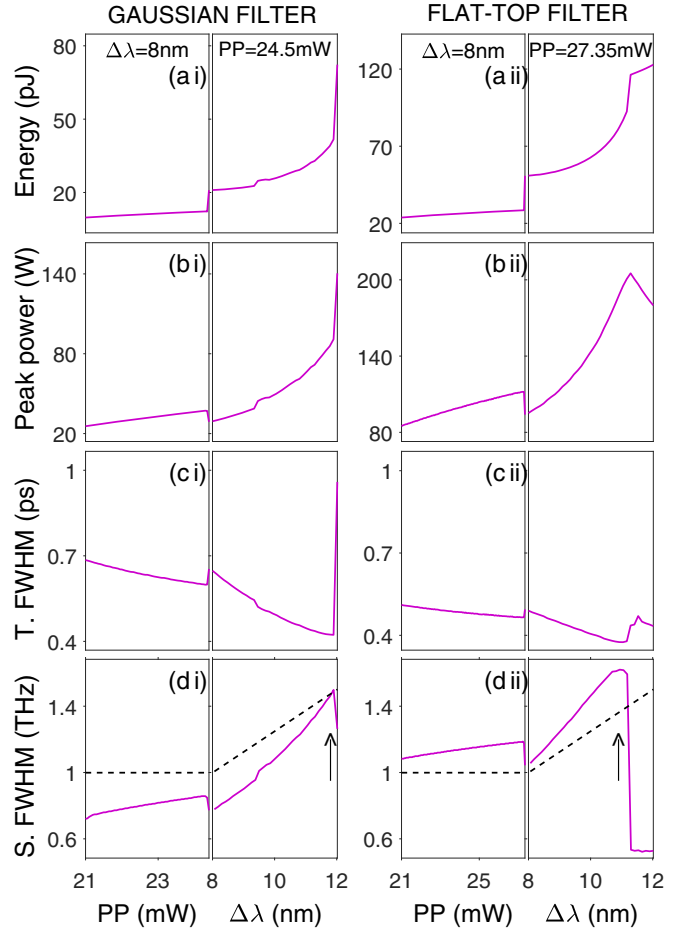


FIG. 10. Evolution of the pulse parameters during the 2D procedure shown in Figs. 8(a i) and 8(a ii): (a i) and (a ii) pulse energy, (b i) and (b ii) pulse peak power, (c i) and (c ii) temporal FWHM, and (d i) and (d ii) spectral FWHM.

also adopt a spectral profile that minimizes the attenuation produced by the BPF. To gain insight into the role of the BPF in a defragmentation process, we have examined the evolution of the pulse parameters during the 2D process considered in Figs. 8(a i) and 8(a ii), in which the second step of the 2D process begins just after the fragmentation of the pulse generated in the first step of the process. Figure 10 shows the pulse parameters at the filter input as a function of the PP in the first phase of the process and as a function of the filter bandwidth in the second phase of the process. The following general characteristics are observed.

(i) Pulse parameters change gradually (helped in that because we vary the configuration parameters gradually to keep the evolution adiabatic), except at two specific moments which are nothing other than the times when fragmentation and defragmentation occur. As the fragmentation phenomenon has already been addressed as part of the conventional approach, hereafter we focus on the defragmentation process. Figure 10 shows that during the first phase of the process, some pulse parameters grow monotonically (energy, peak power, and spectral width) while the temporal width decreases monotonically. At the end of the first phase, fragmentation occurs and causes an abrupt variation in all pulse

parameters. It is quite remarkable that, in the second phase of the process, all pulse parameters continue to vary in the same direction as in the first phase, but in a more pronounced way. Thus, the pulse spectrum, which widened only moderately in the first phase of the process, continues to broaden in the second phase but at a faster rate, with the peculiarity that this rate is higher than the rate of widening of the BPF bandwidth [indicated by the dashed lines in Figs. 10(d i) and 10(d ii)]. Consequently, in the cavity equipped with a Gaussian filter, the pulse spectrum, which was initially within the bandwidth limits, widens to the bandwidth limits. Defragmentation occurs when the pulse spectrum begins to overflow the bandwidth, as indicated by the small arrow in Fig. 10(d i). The action of the filter, which is then at its peak, completely destabilizes the multipulse state and causes a restructuring of the intensity profile, resulting in a containment of the pulse spectrum within the bandwidth limits. In fact, this restructuring of the pulse profile corresponds to a relaxation process because the resulting spectral containment is so strong that the resulting pulse is in a state where the influence of the filter is negligible. The relaxation process also occurs in the cavity equipped with the flat-top filter, as can be seen in Fig. 10(d ii), but it is preceded by a phenomenology that differs drastically from that described for the Gaussian filter. Indeed, at the beginning of the second phase of the 2D procedure (i.e., at $\Delta\lambda = 8$ nm) in the cavity equipped with the flat-top filter, the pulse spectrum is already slightly overflowing from the filter bandwidth. As $\Delta\lambda$ increases, this overflow increases to the peak of the filter destabilizing effect, where defragmentation occurs.

Furthermore, it is worth noting in Figs. 8 and 9 that the 2D approach under study has an obvious interest, which is to significantly reduce the level of PP required to access the multipulse regime. Another major advantage of this approach is the multitude of routes it offers to access the multipulse regime. For example, Fig. 11 shows the result we get by following a different route from that of Fig. 8, to access the multipulse regime for $\Delta\lambda = 12$ nm. In Fig. 11 we use a 2D approach where the first step starts with $\Delta\lambda_{\text{opt}} = 4$ nm. Figures 11(a i) and 11(a ii) show the result obtained when the first step of the procedure ends just after the fragmentation point, i.e., at a PP of 25.45 mW (30 mW) for the Gaussian (flat-top) filter. Figures 11(b i) and 11(b ii) show the result obtained for a PP slightly above the fragmentation point, while Figs. 11(c i) and 11(c ii) correspond to the case where the PP is slightly below the fragmentation point. Figure 12 gives a better overview of the intensity profile of the multipulse structure generated at the end of the 2D procedure displayed in Figs. 11(b i) and 11(b ii). It is clear that the results of Figs. 11 and 12 have the same general following characteristics as those of Figs. 8 and 9.

(i) Three (two) pulses are generated in the cavity equipped with the Gaussian (flat-top) filter.

(ii) The pulses generated with the Gaussian filter are physically identical, while those generated with the flat-top filter have different characteristics.

(iii) The spectrum of the final multipulse structure occupies almost the entire bandwidth of the filter, as shown in Figs. 9(b) and 12(b), thus indicating that, regardless of its bandwidth and its spectral profile, the filter plays a decisive

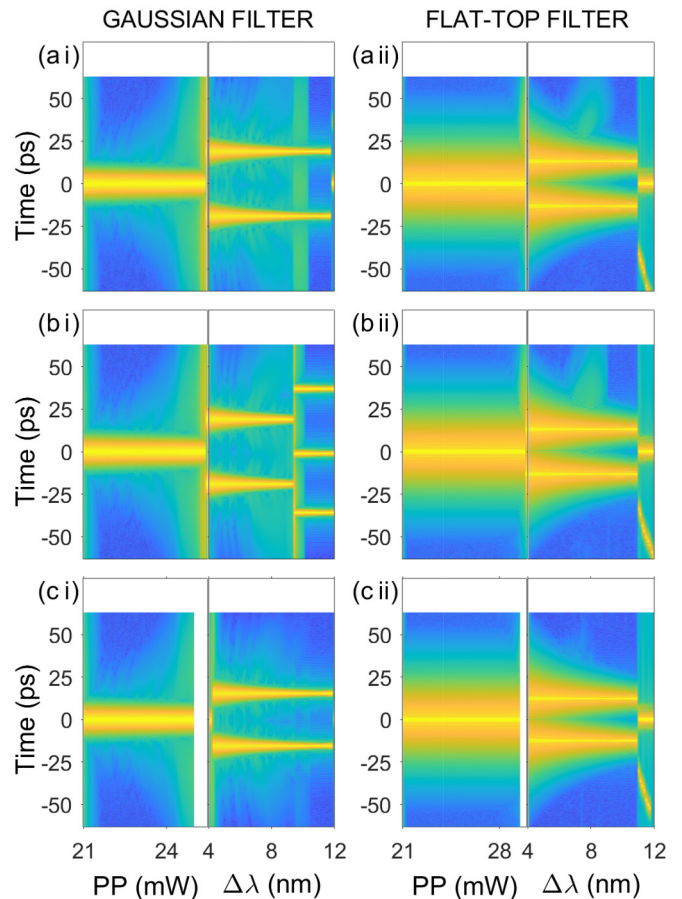


FIG. 11. Evolution of the 2D contour of the temporal intensity as a function of the pumping power for $\Delta\lambda = 4$ nm (first step) and according to the bandwidth of the filter (second step): (a) final PP set just after the fragmentation point at (a i) 25.45 mW and (a ii) 30 mW, (b) final PP set slightly above the fragmentation point at (b i) 25.5 mW and (b ii) 30.05 mW, and (c) final PP set slightly below the fragmentation point at (c i) 25 mW and (c ii) 29.5 mW.

role in the 2D procedure of access to the multipulse regime whereas in the conventional approach the filter plays almost no role when $\Delta\lambda > \Delta\lambda_c$. Thus, the aforementioned general characteristics clearly indicate that the two routes we have chosen to access the multipulse regime lead to two states located in the immediate vicinity of the same fixed point (of the laser dynamics), with which they share the same general characteristics. The two states show only small differences in their temporal profiles, because of the slight difference in the respective PPs used in the two routes to the multipulse regime.

In the following, we focus on a striking simulation result appearing in Figs. 9 and 12, namely, the asymmetry between the two pulses generated by the cavity equipped with a flat-top filter after the filter bandwidth has been increased to 12 nm. Indeed, we initially expect that the shape of all pulses traveling round the laser cavity would be identical, defined by a common dissipative soliton attractor [9]. The simultaneous propagation of pulses with different profiles is rather exceptional, requiring specific laser cavity parameters [47]. Note that in the latter case, pulses having different profiles are expected to travel at different velocities, unless they form a

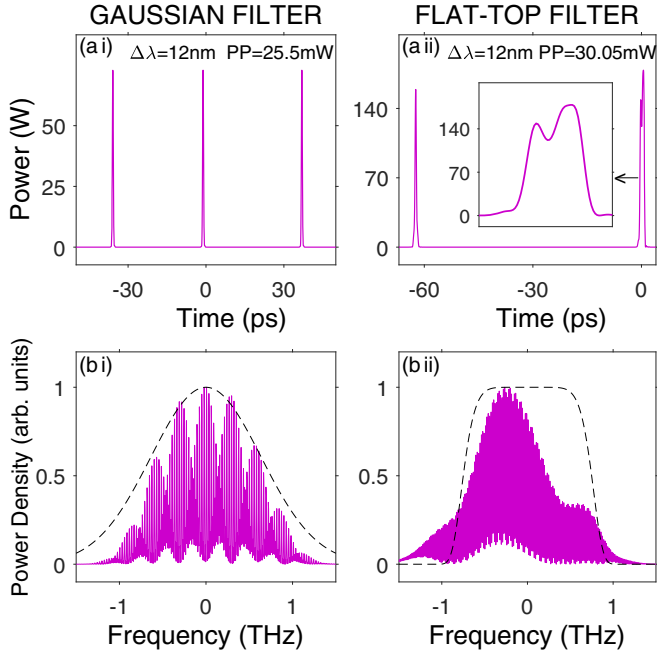


FIG. 12. Multipulse intensity profile generated at the end of the two-dimensional procedure shown in Figs. 11(b i) and 11(a ii): (a i) and (a ii) temporal profile and (b i) and (b ii) spectral profile.

compact composite soliton molecule. A close examination of the second phase of the 2D process displayed in Figs. 8 and 11 leads us to attribute this asymmetry between the two pulses to the hybridization of the defragmentation process with other phenomena involved in laser dynamics. Indeed, we define a perfect defragmentation process as a process that generates a state where the pulses are less numerous but all identical. On the other hand, we see in Figs. 8 and 11 that after this process of *hybrid defragmentation*, which occurs for a value of $\Delta\lambda$ between 11 and 12 nm, the less intense pulse drifts in the temporal domain monotonically as that $\Delta\lambda$ approaches 12 nm. We attribute this temporal drift to the combined action of several phenomena, among which stimulated Raman scattering (SRS) is likely to play the key role [46,48,49]. Indeed, SRS comes into play because of the relatively high peak power of the two pulses (approximately 100 W) and the difference in peak power between the two pulses [as can be seen in Figs. 9(a ii) and 12(a ii)]. To identify the other phenomena involved in the pulse temporal drift, it is preferable to set up a variational analysis of the GNLSE, which is the best way to determine the specific mode of action of each term of the equation on the pulse's intensity and phase profiles. However, the GNLSE (1) contains terms that are not mathematically practical to deal with in a variational analysis, foremost among which are the terms representing a lumped effect at any point in the cavity specified by the z distance coordinate (e.g., the filtering effect) and the Raman scattering term that produces delayed effects. It is therefore necessary to mathematically reformulate those terms before performing the variational analysis. Thus, the lumped filtering can be approximated by an equivalent continuous distributed filtering action along the cavity, defined by $F[\psi] \equiv \xi \psi_{tt}$, where ξ is a constant that depends on the spectral profile of the BPF

and the length of the cavity [48,49]. On the other hand, by neglecting the TOD and using the linear approximation of $\tilde{\chi}_R$, the nonlinear Schrödinger equation takes the form [48,49]

$$\begin{aligned} \psi_z + \frac{i\beta_2(z)}{2} \psi_{tt} + \frac{\alpha(z)}{2} \psi - i\gamma|\psi|^2\psi \\ = \xi \psi_{tt} + i\gamma\rho f_1 \psi \frac{\partial|\psi|^2}{\partial t}. \end{aligned} \quad (3)$$

The last term in Eq. (3) represents the Raman contribution, with $f_1 \approx 7 \times 10^{-3}$ a typical value [49]. To obtain a qualitative idea of the internal dynamics of the pulse, we assume a Gaussian ansatz given by

$$\psi_g = x_1 \exp\left(-\eta^2/x_3^2 + ix_4\eta^2/2 + ix_5\eta + ix_6\right), \quad (4)$$

where $\eta = t - x_2$ and $x_1, x_2, \sqrt{2\ln 2}x_3, x_4/2\pi, x_5/2\pi$, and x_6 represent the pulse's amplitude, temporal position, width (FWHM), chirp, frequency, and phase, respectively. Then, following a collective-variable approach [49], we obtain the explicit analytical expressions for the dynamics of the pulse parameters

$$\dot{x}_1 = -\frac{\alpha x_1}{2} + \frac{\beta_2 x_1 x_4}{2} - x_1(x_5^2 + 2x_3^{-2})\xi, \quad (5)$$

$$\dot{x}_2 = -\beta_2 x_5 - x_4 x_3^2 x_5 \xi, \quad (6)$$

$$\dot{x}_3 = -\beta_2 x_3 x_4 + \frac{(4 - x_3^4 x_4^2) x_3^{-2} \xi}{2}, \quad (7)$$

$$\dot{x}_4 = -(4 - x_3^4 x_4^2) x_3^{-4} \beta_2 - \sqrt{2} x_1^2 x_3^{-2} \gamma - 8 x_4 x_3^{-2} \xi, \quad (8)$$

$$\dot{x}_5 = -\sqrt{2} \gamma x_1^2 x_3^{-2} - x_5(4 x_3^{-2} + x_3^2 x_4^2) \xi, \quad (9)$$

$$\dot{x}_6 = -\frac{\beta_2}{2}(x_5^2 - 2x_3^{-2}) + \frac{5\sqrt{2}\gamma}{8} x_1^2 + (1 - x_3^2 x_4^2) x_4 \xi, \quad (10)$$

where $\gamma_r = \rho f_1$. Here we do not intend to solve numerically the above variational equations, but rather to use them to analyze and identify the different effects that contribute to the temporal drift of certain pulses. Let us consider the internal dynamics of a pulse, where the initial condition is chosen to be a free-chirp point of the cavity, i.e., $x_4(z=0) = 0$. Suppose that at $z=0$ the pulse's spectrum is located exactly at the center of the bandwidth of the system, i.e., with no frequency shift $x_5(z=0) = 0$. Then the first term on the right-hand side of Eq. (9) indicates that SRS causes the pulse spectrum to drift continuously towards low frequencies at a rate proportional to the pulse's peak power (x_1^2) and inversely proportional to the square of its temporal width (x_3^2). The second term on the right-hand side of Eq. (9), which is proportional to the resulting frequency shift $x_5 \neq 0$, triggers one of the filtering effects, which is to oppose any frequency drift. Thus, the spectral filter imposes a limit on the drift caused by SRS, but does not bring the pulse's spectrum back to the center of the bandwidth. When this limit is reached, the corresponding spectral shift is converted into a temporal shift by the chromatic dispersion of the intracavity fiber system, as shown by the first term on the right-hand side of Eq. (6). However, in a dispersion-compensated cavity such as the one considered in the present study, the temporal shifts (x_2) occur in opposite directions $x_2 > 0$ or $x_2 < 0$, depending on whether the

pulse propagates in a fiber section with positive ($\beta_2 > 0$) or negative ($\beta_2 < 0$) dispersion, which should lead globally to a zero temporal shift after a complete cavity round-trip. The second term on the right-hand side of Eq. (6) shows that the filter also converts the pulse's frequency shift into a temporal shift, but the cavity has no mechanism to compensate for this temporal shift. Thus, the difference in peak power between the two pulses generated in the cavity equipped with the flat-top filter [see Figs. 9(a ii) and 12(a ii)] leads to a difference in their respective Raman-induced frequency shifts, which is converted into a difference in their respective drift speeds in the temporal domain.

V. CONCLUSION

In this study we have analyzed the strategies of access to the multipulse regime of a MLFL and showed that the operational conditions for generating stable multipulse structures can be dramatically improved by including a tunable-bandwidth spectral filter within the laser cavity. Our analysis shows that an adequate spectral filter setting results in a drastic reduction in the PP needed to access the multipulse regime, of typically 50% for the laser cavity configuration we have considered. We have shown that the conventional procedure of reaching the multipulse operation through the sole increase of the PP is effective only when the filter bandwidth ($\Delta\lambda$) is small enough, i.e., below a critical value $\Delta\lambda_c$ which depends on the configuration of the other cavity components. On the other hand, for $\Delta\lambda > \Delta\lambda_c$ the conventional method is inefficient because the level of PP required to generate multipulse structures is significantly higher than that of the region where $\Delta\lambda < \Delta\lambda_c$ and the intensity profiles of the generated pulses are affected by important distortions with respect to a bell-shaped profile.

One of the most important results of the present study is the development of a 2D parameter adjustment procedure that avoids the disadvantages of the conventional approach.

To generate multipulse structures via the 2D approach with a bandwidth $\Delta\lambda > \Delta\lambda_c$, we proceed in two steps. First, we set the bandwidth value to $\Delta\lambda_{\text{opt}} < \Delta\lambda_c$ and we gradually increase the PP to a level slightly above the fragmentation point. At the end of this step, the laser is in multipulse regime, with a relatively low PP, but with a bandwidth $\Delta\lambda_{\text{opt}}$ which is not the desired bandwidth. The second step of the procedure is to gradually increase the bandwidth up to the desired value $\Delta\lambda$ by keeping the PP at a level slightly above the fragmentation point. Using this two-dimensional method, we have succeeded in generating multipulse structures with distortion-free pulse profiles and with a PP level as low as those required in the region where $\Delta\lambda < \Delta\lambda_c$.

Furthermore, the present study reveals major qualitative differences in the intensity profile of the stable states, depending on whether the cavity is equipped with a Gaussian or flat-top filter. The flat-top filter promotes the generation of pulses with higher peak power, which in turn exacerbate nonlinear effects and instability phenomena such as defragmentation, distortions of pulse intensity profile, and pulse temporal drift phenomena induced by Raman scattering and chromatic dispersion of intracavity fibers. Despite the increase in the complexity of pulse dynamics in the latter case, we have shown that the analysis of the dynamics of multipulse structures remains possible using collective coordinate methods.

Finally, our 2D approach of the present work offers possibilities for access to various types of multipulse structures, including bound states of solitons such as soliton molecules, macromolecules, and complex molecular or soliton crystals.

ACKNOWLEDGMENTS

We acknowledge support from the Conseil Régional de Bourgogne-Franche-Comté, iXCore Research Foundation, and Agence Nationale de la Recherche (through Projects No. ANR-15-IDEX-0003 and No. ANR-17-EURE-0002).

-
- [1] D. Y. Tang, W. S. Man, H. Y. Tam, and P. D. Drummond, Observation of bound states of solitons in a passively mode-locked fiber laser, *Phys. Rev. A* **64**, 033814 (2001).
 - [2] P. Grelu, F. Belhache, F. Gutty, and J. M. Soto-Crespo, Phase-locked soliton pairs in a stretched-pulse fiber laser, *Opt. Lett.* **27**, 966 (2002).
 - [3] M. Stratmann, T. Pagel, and F. Mitschke, Experimental Observation of Temporal Soliton Molecules, *Phys. Rev. Lett.* **95**, 143902 (2005).
 - [4] B. Ortaç, A. Zaviyalov, C. K. Nielsen, O. Egorov, R. Iliew, J. Limpert, F. Lederer, and A. Tünnermann, Observation of soliton molecules with independently evolving phase in a mode-locked fiber laser, *Opt. Lett.* **35**, 1578 (2010).
 - [5] K. Krupa, K. Nithyanandan, U. Andral, P. Tchofo-Dinda, and P. Grelu, Real-Time Observation of Internal Motion within Ultrafast Dissipative Optical Soliton Molecules, *Phys. Rev. Lett.* **118**, 243901 (2017).
 - [6] M. Liu, H. Li, A.-P. Luo, H. Cui, W.-C. Xu, and Z.-C. Luo, Real-time visualization of soliton molecules with evolving behavior in an ultrafast fiber laser, *J. Opt.* **20**, 034010 (2018).
 - [7] D. Zou, Y. Song, O. Gat, M. Hu, and P. Grelu, Synchronization of the internal dynamics of optical soliton molecules, *Optica* **9**, 1307 (2022).
 - [8] F. Amrani, M. Salhi, P. Grelu, H. Leblond, and F. Sanchez, Universal soliton pattern formations in passively mode-locked fiber lasers, *Opt. Lett.* **36**, 1545 (2011).
 - [9] P. Grelu and N. Akhmediev, Dissipative solitons for mode-locked lasers, *Nat. Photon.* **6**, 84 (2012).
 - [10] Z. Wen, W. Wang, S. Gao, K. Wang, Y. Cai, and Y. Gao, Soliton macromolecule dynamics in fiber lasers with sinusoidal filtered nonlinear optical loop mirror, *Phys. Rev. A* **106**, 023522 (2022).
 - [11] Z. Wang, K. Nithyanandan, A. Coillet, P. Tchofo-Dinda, and P. Grelu, Optical soliton molecular complexes in a passively mode-locked fibre laser, *Nat. Commun.* **10**, 830 (2019).
 - [12] W. He, M. Pang, D.-H. Yeh, J. Huang, and P. S. J. Russell, Synthesis and dissociation of soliton molecules in parallel optical-soliton reactors, *Light Sci. Appl.* **10**, 120 (2021).
 - [13] A. Komarov, A. Haboucha, and F. Sanchez, Ultrahigh-repetition-rate bound-soliton harmonic passive mode-locked fiber lasers, *Opt. Lett.* **33**, 2254 (2008).

- [14] A. Andrianov and A. Kim, Widely stretchable soliton crystals in a passively mode-locked fiber laser, *Opt. Express* **29**, 25202 (2021).
- [15] J. Girardot, A. Coillet, M. Nafa, F. Billard, E. Hertz, and P. Grelu, On-demand generation of soliton molecules through evolutionary algorithm optimization, *Opt. Lett.* **47**, 134 (2022).
- [16] S. Liu, Y. Cui, E. Karimi, and B. A. Malomed, On-demand harnessing of photonic soliton molecules, *Optica* **9**, 240 (2022).
- [17] C. Lecaplain and P. Grelu, Multi-gigahertz repetition-rate-selectable passive harmonic mode locking of a fiber laser, *Opt. Express* **21**, 10897 (2013).
- [18] Q. Huang, L. Dai, A. Rozhin, M. A. Araimi, and C. Mou, Non-linearity managed passively harmonic mode-locked Er-doped fiber laser based on carbon nanotube film, *Opt. Lett.* **46**, 2638 (2021).
- [19] A. K. Komarov and K. P. Komarov, Multistability and hysteresis phenomena in passive mode-locked lasers, *Phys. Rev. E* **62**, R7607 (2000).
- [20] A. Komarov, H. Leblond, and F. Sanchez, Multistability and hysteresis phenomena in passively mode-locked fiber lasers, *Phys. Rev. A* **71**, 053809 (2005).
- [21] F. Li, P. K. A. Wai, and J. N. Kutz, Geometrical description of the onset of multi-pulsing in mode-locked laser cavities, *J. Opt. Soc. Am. B* **27**, 2068 (2010).
- [22] M. Alsaleh, C. B. L. Mback, E. T. Felenou, P. Tchofo Dinda, P. Grelu, and K. Porsezian, Strength and weaknesses of modeling the dynamics of mode-locked lasers by means of collective coordinates, *J. Opt.* **18**, 075501 (2016).
- [23] M. Alsaleh, T. Uthayakumar, E. Tchomgo-Felenou, P. Tchofo Dinda, P. Grelu, and K. Porsezian, Pulse breaking through spectral filtering in dispersion-managed fiber lasers, *J. Opt. Soc. Am. B* **35**, 276 (2018).
- [24] X. Zhang, F. Li, K. Nakkeeran, J. Yuan, Z. Kang, J. N. Kutz, and P. K. A. Wai, Impact of spectral filtering on multipulsing instability in mode-locked fiber lasers, *IEEE J. Sel. Top. Quantum Electron.* **24**, 1 (2018).
- [25] J. Igbonacho, K. Nithyanandan, K. Krupa, P. Tchofo Dinda, P. Grelu, and A. B. Moubissi, Dynamics of distorted and undistorted soliton molecules in a mode-locked fiber laser, *Phys. Rev. A* **99**, 063824 (2019).
- [26] H. A. Haus, J. G. Fujimoto, and E. P. Ippen, Structures for additive pulse mode locking, *J. Opt. Soc. Am. B* **8**, 2068 (1991).
- [27] S. Chouli, J. M. Soto-Crespo, and P. Grelu, Optical spectra beyond the amplifier bandwidth limitation in dispersion-managed mode-locked fiber lasers, *Opt. Express* **19**, 2959 (2011).
- [28] A. Chong, W. H. Renninger, and F. W. Wise, All-normal-dispersion femtosecond fiber laser with pulse energy above 20 nJ, *Opt. Lett.* **32**, 2408 (2007).
- [29] K. Regelskis, J. Želudevičius, K. Viskontas, and G. Račiukaitis, Ytterbium-doped fiber ultrashort pulse generator based on self-phase modulation and alternating spectral filtering, *Opt. Lett.* **40**, 5255 (2015).
- [30] Z. Wen, B. Lu, X. Qi, C. Zhang, K. Wang, H. Chen, and J. Bai, Effects of spectral filtering on pulse dynamics in a mode-locked fiber laser with a bandwidth tunable filter, *J. Opt. Soc. Am. B* **36**, 952 (2019).
- [31] D. Yan, B. Liu, D. Zou, J. Guo, Y. Chu, Y. Song, and M. Hu, Spectral filtering effect on multi-pulsing induced by chirped fiber Bragg grating in dispersion-managed mode-locked Yb-doped fiber lasers, *High Power Laser Sci. Eng.* **9**, e46 (2021).
- [32] F. Wang, A. G. Rozhin, V. Scardaci, Z. Sun, F. Hennrich, I. H. White, W. I. Milne, and A. C. Ferrari, Wideband-tuneable, nanotube mode-locked, fibre laser, *Nat. Nanotechnol.* **3**, 738 (2008).
- [33] K. Tamura, E. Ippen, and H. Haus, Optimization of filtering in soliton fiber lasers, *IEEE Photon. Technol. Lett.* **6**, 1433 (1994).
- [34] X. Liu and Y. Cui, Flexible pulse-controlled fiber laser, *Sci. Rep.* **5**, 9399 (2015).
- [35] D. Li, H. Jussila, Y. Wang, G. Hu, T. Albrow-Owen, R. C. T. Howe, Z. Ren, J. Bai, T. Hasan, and Z. Sun, Wavelength and pulse duration tunable ultrafast fiber laser mode-locked with carbon nanotubes, *Sci. Rep.* **8**, 2738 (2018).
- [36] Y. S. Fedotov, S. M. Kobtsev, R. N. Arif, A. G. Rozhin, C. Mou, and S. K. Turitsyn, Spectrum-, pulsewidth-, and wavelength-switchable all-fiber mode-locked Yb laser with fiber based birefringent filter, *Opt. Express* **20**, 17797 (2012).
- [37] S. Boscolo, J. Peng, and C. Finot, Design and applications of in-cavity pulse shaping by spectral sculpturing in mode-locked fibre lasers, *Appl. Sci.* **5**, 1379 (2015).
- [38] D. Li, D. Tang, L. Zhao, and D. Shen, Mechanism of dissipative-soliton-resonance generation in passively mode-locked all-normal-dispersion fiber lasers, *J. Lightw. Technol.* **33**, 3781 (2015).
- [39] Z. Wang, L. Zhan, X. Fang, and H. Luo, Spectral filtering effect on mode-locking regimes transition: Similariton-dissipative soliton fiber laser, *J. Opt. Soc. Am. B* **34**, 2325 (2017).
- [40] J. Schröder, S. Coen, T. Sylvestre, and B. J. Eggleton, Dark and bright pulse passive mode-locked laser with in-cavity pulse-shaper, *Opt. Express* **18**, 22715 (2010).
- [41] S. Boscolo, C. Finot, H. Karakuzu, and P. Petropoulos, Pulse shaping in mode-locked fiber lasers by in-cavity spectral filter, *Opt. Lett.* **39**, 438 (2014).
- [42] Y. Du and X. Shu, Pulse dynamics in all-normal dispersion ultrafast fiber lasers, *J. Opt. Soc. Am. B* **34**, 553 (2017).
- [43] J. Peng and S. Boscolo, Filter-based dispersion-managed versatile ultrafast fibre laser, *Sci. Rep.* **6**, 25995 (2016).
- [44] B. D. Gupta, S. D. Chowdhury, D. Dhirhe, and M. Pal, Intermittent events due to spectral filtering induced multi-pulsing instability in a mode-locked fiber laser, *J. Opt. Soc. Am. B* **37**, 2278 (2020).
- [45] G. P. Agrawal, *Nonlinear Fiber Optics* (Elsevier, Amsterdam, 2012).
- [46] T. Uthayakumar, M. Alsaleh, J. Igbonacho, E. T. Felenou, P. Tchofo Dinda, P. Grelu, and K. Porsezian, Impact of Raman scattering on pulse dynamics in a fiber laser with narrow gain bandwidth, *J. Opt.* **20**, 065502 (2018).
- [47] J. M. Soto-Crespo, M. Grapinet, P. Grelu, and N. Akhmediev, Bifurcations and multiple-period soliton pulsations in a passively mode-locked fiber laser, *Phys. Rev. E* **70**, 066612 (2004).
- [48] P. Tchofo Dinda, K. Nakkeeran, and A. Labruyere, Suppression of soliton self-frequency shift by upshifted filtering, *Opt. Lett.* **27**, 382 (2002).
- [49] P. Tchofo Dinda, A. Labruyere, and K. Nakkeeran, Theory of Raman effect on solitons in optical fibre systems: Impact and control processes for high-speed long-distance transmission lines, *Opt. Commun.* **234**, 137 (2004).